POLITECNICO DI TORINO
Repository ISTITUZIONALE

Assessment of the AUSM Scheme for Near-Nozzle Flow Field Characterization of Under-Expanded Hydrogen Jets

Original
Assessment of the AUSM Scheme for Near-Nozzle Flow Field Characterization of Under-Expanded Hydrogen Jets / Vento, O., Baronetto, C., Ferrari, A.. - In: ENERGIES. - ISSN 1996-1073. - 19:8(2026). [10.3390/en19081871]

Availability:
This version is available at: 11583/3010833 since: 2026-05-14T12:03:24Z

Publisher:
MDPI

Published
DOI:10.3390/en19081871

Terms of use:

This article is made available under terms and conditions as specified in the corresponding bibliographic description in the repository

Publisher copyright

(Article begins on next page)

05 November 2026

energies

MDPI

Article

Assessment of the AUSM Scheme for Near-Nozzle Flow Field Characterization of Under-Expanded Hydrogen Jets

Oscar Vento *, Carmelo Baronetto and Alessandro Ferrari

Energy Department, Politecnico di Torino, Corso Duca degli Abruzzi, 24, 10129 Torino, Italy; carmelo.baronetto@polito.it (C.B.); alessandro.ferrari@polito.it (A.F.)
* Correspondence: oscar.vento@polito.it

Abstract

Hydrogen is a carbon-free energy carrier that can support decarbonization of the energy and transport systems. Its usage as a fuel in internal combustion engines can abate the pollutants and CO_2 emissions but also presents various challenges. Among these, the formation of under-expanded jets requires proper injector design and accurate control of the injection process. CFD can accelerate the development of hydrogen engine technologies towards market readiness. Low-dissipative density-based schemes are essential to accurately describe the complex flow structures, that affect mixture formation in under-expanded injections. In the present work, the AUSM scheme was implemented in the OpenFOAM library, and successfully used to simulate an experimental hydrogen-into-nitrogen injection. The numerical method, validated against experimental Schlieren images, was compared with the Kurganov–Noelle–Petrova scheme implemented in the current density-based OpenFOAM solver. The numerical results highlighted the reduced dissipation of the AUSM scheme, leading to improved jet penetration and gas mixing. The investigation demonstrated the superior performance of the AUSM scheme, suggesting it as an alternative OpenFOAM solver. Nevertheless, the study identified areas for improvement and critical issues associated with this type of simulations.

Keywords: OpenFOAM; hydrogen injection; under-expanded jets; AUSM scheme

1. Introduction

The growing demand for low-carbon energy solutions has gained increasing interest in hydrogen (H_2) as an alternative fuel that can help internal combustion engines (ICEs) to meet the increasingly strict EU regulations [1]. Hydrogen is carbon-free; thus, H_2-fueled ICEs (H2ICEs) are not subject to HC, CO and CO_2 emissions, while using a suitable lubricating oil can prevent emissions associated with its combustion [1,2]. H2ICEs represent a near-term solution to decarbonization and emission challenges since they allow the retrofitting of conventional ICEs [3] and can leverage existing ICE know-how as well as established large-scale manufacturing and supply chains [4]. The NO_x emissions that can potentially affect H2ICEs, can be brought close to zero by adopting ultra-lean combustion strategies. This is possible due to the wide range of flammability of hydrogen (air–fuel equivalence ratio, namely λ, from 0.14 to 10), as the excess air in the mixture reduces the combustion temperature, thereby suppressing NO_x formation. The low engine power, due to the ultra-lean mixture and the low density of gaseous hydrogen, requires supercharging combined with direct injection (DI) to achieve comparable power output to current state-of-the-art conventional ICEs [4]. While supercharging increases the air

Check for updates

Academic Editor: Nadir Yilmaz

Received: 13 March 2026
Revised: 2 April 2026
Accepted: 5 April 2026
Published: 11 April 2026

Copyright: © 2026 by the authors. Licensee MDPI, Basel, Switzerland. This article is an open access article distributed under the terms and conditions of the Creative Commons Attribution (CC BY) license.

mass in the cylinder without enlarging the engine displacement, DI improves the engine volumetric efficiency compared to port fuel injection (PFI), preventing air displacement by the low-density hydrogen in the intake manifold. In addition, DI eliminates backfiring as injection occurs after the intake valve closure (IVC) and enables the stratification of the charge. Specifically, it is possible to obtain a richer mixture close to the spark plug, that gets progressively leaner close to the cylinder walls. Charge stratification reduces pumping losses and wall heat transfer, improving the engine efficiency, and also lowers the risk of pre-ignition [1]. Hydrogen injectors are frequently derived from modified gasoline direct injectors [5–9], featuring pressures of 20–30 bar for low-pressure DI (LPDI) and above 100 bar for high-pressure DI (HPDI) [10]. These pressure levels enable late-injection strategies, in which fuel is delivered within a very short time window during the final phase of the compression stroke, when the in-cylinder pressure is high. In both LP- and HPDI applications, the H_2 jet is typically under-expanded because the ratio of total pressure upstream of the injector nozzle to in-cylinder static pressure exceeds a threshold value. The threshold ratio depends on the gas and on the geometry considered, including circular orifices and rectangular slots, as reported in [11]. For hydrogen jets issuing from a circular orifice, this threshold pressure ratio is approximately 3.85 [12]. Therefore, the hydrogen jet in H2ICEs is characterized by complex phenomena, including gas dynamics shocks and the Mach disk, that strongly affect key parameters of the injection, such as mass flow rate, jet tip penetration, and jet cone angle. The understanding of how under-expansion influences the mixture formation, and consequently the performance and efficiency of the engine, is fundamental for the design of H2ICEs [13]. Although fundamental, experimental studies on hydrogen are currently restricted to a limited range of configurations and operating conditions [13]. In this context, CFD is a relevant tool that, once validated against the available experimental data, can improve the comprehension of under-expanded hydrogen jets [4], and more generally support the development of ICEs [3,14]. Numerical simulations of under-expanded jets are typically compared against experimental Schlieren images of the near-nozzle field [15–19], and other relevant quantities such as the injected mass flow rate. The Mach disk position can also be validated against empirical correlations of its distance from the nozzle outlet [20]. The evaluation of jet penetration is less commonly addressed in the literature. A study of this kind, which investigates the effects of jet caps mounted at the top of the injector, is presented in [3]. CFD is also economically convenient compared to not easily reconfigurable experimental apparatus, and it also provides the quantitative measurement of air–fuel mixing and the in-cylinder temperature field, that are difficult to be obtained experimentally [21]. In the presence of gas-dynamic shocks, as is the case for under-expanded jets, density-based schemes outperform pressure-based ones, which had been originally developed for incompressible flows [15]. Furthermore, the complex jet structure requires increasing the scheme accuracy. This is achieved in space through either slope limiters, which linearly reconstructs the numerical solution, or high order Weighted Essentially Non Oscillatoraty (WENO) polynomials [22]. The accuracy in time is accordingly increased by using Runge–Kutta algorithms that can be easily constructed in the case of explicit schemes [16,23]. A very fine mesh is mandatory to accurately capture the jet structure and the Mach disk, and it enables Large Eddy Simulation (LES) for turbulence modeling [15,17–19]. Since the Mach disk and other small-scale phenomena are confined to a small portion of the computational domain, Adaptive Mesh Refinement (AMR) can be effectively used to reduce the computational cost of the simulations [19]. The Advection Upstream Splitting Methods (AUSM), including the original AUSM [24] and its variants AUSM$^+$ [25] and AUSM$^+$-up [26], are particularly attractive because they provide: (i) robust and accurate solutions for gas-dynamic shocks, (ii) applicability over a wide range of Mach numbers (for AUSM$^+$-up), and (iii) straightforward extension to

real gas models, since they do not require diagonalization of the governing system of equations [27]. The AUSM scheme was used as reference in numerical studies of supersonic air jets in both two- and three-dimensional axisymmetric domains [28], as well as to investigate the acoustic characteristics of supersonic planar jets [29]. AUSM$^+$ and AUSM$^+$-up have demonstrated good performance in simulating multi-species under-expanded jets. Specifically, under-expanded hydrogen and methane jets were successfully simulated in [17–19], analyzing how pressure ratio and ambient pressure affect key injection features, such as jet penetration, mixture formation, and the near-nozzle flow field. The AUSM$^+$-up, implemented in a hybrid scheme [30], accurately described the Richtmyer–Meshkov instabilities in multi-species simulations [31]. Moreover, it was used in a reactive solver designed for detonation problems [32]. Within the OpenFOAM framework, simulations of under-expanded jets [15,16] have been predominantly performed using rhoCentralFoam [33]. This solver implements the Kurgnavov–Noelle–Petrova (KNP) scheme [34] and is currently the mainly density-based method of the OpenFOAM library. However, numerical oscillations, especially with the use of aggressive slope limiters, were reported in [28,32,35]. The KNP scheme thus requires very small Courant numbers and it is usually combined with high order Runge–Kutta time scheme, that improve numerical diffusion. In fact, although slope limiters achieve second-order accuracy in space, third- or fourth-order time schemes are typically used; furthermore, numerical oscillations were also observed without slope limiters. At the same time, studies [28,32] highlighted the reduced diffusion of AUSM schemes, which can accurately describe shocks and vortices. The aim of the present work is to assess the accuracy of the AUSM scheme in reproducing an experimental H_2 injection [12] and to compare its performance with that of the KNP scheme. The AUSM scheme, implemented in a OpenFOAM solver, was preferred over the AUSM$^+$ and AUSM$^+$-up since these schemes are mainly intended for low Mach number flows, which are not relevant here. This investigation includes model validation against experimental data as well as the analysis of the numerical results from both schemes.

2. Numerical Methodology

2.1. Governing Equations

The governing equations of compressible flows, including the partial differential equations of mass conservation, momentum balance, and energy conservation, can be written as:

$$\frac{\partial \rho}{\partial t} + \nabla \cdot (\rho \mathbf{U}) = 0 \tag{1}$$

$$\frac{\partial (\rho \mathbf{U})}{\partial t} + \nabla \cdot (\rho \mathbf{U} \otimes \mathbf{U} + p[I]) = \nabla \cdot [\sigma] \tag{2}$$

$$\frac{\partial (\rho e_t)}{\partial t} + \nabla \cdot ((\rho e_t + p)\mathbf{U}) = \nabla \cdot ([\sigma] \cdot \mathbf{U}) - \nabla \cdot \boldsymbol{\mathcal{Q}} \tag{3}$$

where ρ is the density, $\mathbf{U}$ is the velocity vector and $e_t = e + \frac{1}{2}\|\mathbf{U}\|^2$ is the total internal energy, with e being the internal energy. In the present work, the ideal gas model was adopted and the internal energy is equal to $e = \frac{1}{\gamma - 1}\frac{p}{\rho}$, where $\gamma = \frac{c_p}{c_v}$ is the heat specific ratio. Since the mixture was expected to exceed the temperature range covered by the JANAF polynomials [36], a constant specific heat model was considered (see Table 1). The stress tensor is $[\sigma] = \mu\left(\nabla \mathbf{U} + (\nabla \mathbf{U})^T\right) - \frac{2}{3}\mu(\nabla \cdot \mathbf{U}) \cdot [I]$, while the heat flux is given by the Fourier law as $\boldsymbol{\mathcal{Q}} = -k\nabla T$, where k is the thermal conductivity. The presence of different gaseous species can be taken into account by considering the following transport-diffusion equation for the i-th gas [15]:

$$\frac{\partial (\rho Y_i)}{\partial t} + \nabla \cdot (\rho Y_i \mathbf{U}) = \nabla \cdot (\rho \mathcal{D} \nabla Y_i) \tag{4}$$

where the diffusivity is related to the Schmidt number (Sc) as $\mathcal{D} = \frac{\mu}{\rho Sc}$. The Schmidt number is set to $Sc = 0.7$, following common practice in this type of simulations [21,37]. The viscosity is given by $\mu = \mu_l + \mu_t$, with μ_l and μ_t being the laminar and turbulent viscosity, respectively. The laminar viscosity is obtained from the Sutherland law [38]:

$$\mu_l = A_S \frac{\sqrt{T}}{1 + \frac{T_S}{T}} \tag{5}$$

where A_s and T_S are coefficients specified in Table 1.

Table 1. Thermophysical properties.

Specie	c_p (J/kgK)	A_S (μPa/$\sqrt{\text{K}} \cdot$ s)	T_S (K)
N_2	1040	1.512	120
H_2	14,303	0.6362	72

2.2. Turbulence Modeling

Turbulence is modeled using the Wall-Adaptive Large Eddy (WALE) model proposed by [39], which has been successfully applied in previous similar studies [18,19]. The turbulent viscosity is computed as:

$$\mu_t = (C_w \Delta)^2 \frac{\left(S_{ij}^d S_{ij}^d\right)^{3/2}}{\left(S_{ij} S_{ij}\right)^{5/2} + \left(S_{ij}^d S_{ij}^d\right)^{5/4}} \tag{6}$$

where $C_w = 0.325$ and the filter Δ is related to the mesh size by $\Delta = V^{1/3}$, with V being the volume of the computational cell. S_{ij}^d and S_{ij} are, respectively, the components of the tensors:

$$[S^d] = \text{dev}(\text{sym}(\nabla \mathbf{U} \times \nabla \mathbf{U})) \tag{7}$$

and:

$$[S] = \text{sym}(\nabla \mathbf{U}) \tag{8}$$

2.3. AUSM Scheme

The AUSM scheme [24,40] splits the inviscid fluxes into a convective flux $\mathbf{f}^c$, and a pressure flux $\mathbf{f}^p$. By integrating Equations (1)–(4) over the control volume Ω, the system of equations can be written as:

$$\frac{d}{dt}\overline{\mathbf{q}}(t) = -\frac{1}{\Omega}\int_{\partial\Omega} (\mathbf{f}^c + \mathbf{f}^p) dA + \frac{1}{\Omega}\int_{\partial\Omega} \mathbf{S} dA \tag{9}$$

with $\overline{\mathbf{q}}(t) = \frac{1}{\Omega}\int_\Omega \mathbf{q}(t, V) dV$ and

$$\mathbf{q} = \begin{pmatrix} \rho \\ \rho \mathbf{U} \\ \rho e_t \\ \rho Y_i \end{pmatrix} \quad \mathbf{f}^c = \begin{pmatrix} \rho U \\ \rho \mathbf{U} U \\ \rho h_t U \\ \rho Y_i U \end{pmatrix} \quad \mathbf{f}^p = \begin{pmatrix} 0 \\ p\mathbf{n} \\ 0 \\ 0 \end{pmatrix} \quad \mathbf{S} = \begin{pmatrix} 0 \\ [\sigma] \cdot \mathbf{n} \\ ([\sigma] \cdot \mathbf{U} - \mathbf{q}) \cdot \mathbf{n} \\ \rho D_i \frac{\partial Y_i}{\partial n} \end{pmatrix} \tag{10}$$

The total enthalpy is $h_t = h + \frac{1}{2}\|\mathbf{U}\|^2$, while $U = \mathbf{U} \cdot \mathbf{n}$ is the velocity component along the surface normal direction $\mathbf{n}$. The term $\frac{\partial Y_i}{\partial n} = \nabla Y_i \cdot \mathbf{n}$ represents the directional derivative of

Y_i along $\mathbf{n}$. The surface integrals can be approximated as a summation over the faces of the computational cells, and Equation (9) becomes:

$$\frac{d}{dt}\overline{\mathbf{q}} = -\frac{1}{\Omega}\sum_f \left(\mathbf{f}_f^c + \mathbf{f}_f^p\right) A_f + \frac{1}{\Omega}\sum_f \mathbf{S}_f A_f \tag{11}$$

where:

$$\mathbf{f}_f^c = \begin{pmatrix} \rho_f U_f \\ \rho_f \mathbf{U}_f U_f \\ \rho_f h_{t,f} U_f \\ \rho_f Y_{i,f} U_f \end{pmatrix} \quad \mathbf{f}_f^p = \begin{pmatrix} 0 \\ p_f \mathbf{n} \\ 0 \\ 0 \end{pmatrix} \tag{12}$$

The AUSM rewrites the convective flux in terms of the interface Mach number $M_f = \frac{U_f}{a_f}$, with a_f being the interface sound speed:

$$\mathbf{f}_f^c = M_f \begin{pmatrix} \rho_f a_f \\ \rho_f \mathbf{U}_f a_f \\ \rho_f h_{t,f} a_f \\ \rho_f Y_{i,f} a_f \end{pmatrix} = M_f \hat{\mathbf{f}}^c\left(\mathbf{q}_f\right) \tag{13}$$

The convective flux is finally estimated by upwinding the interface quantities according to:

$$\hat{\mathbf{f}}^c\left(\mathbf{q}_f\right) = \begin{cases} \hat{\mathbf{f}}^c(\mathbf{q}_O) & \text{if } M_f \geq 0 \\ \hat{\mathbf{f}}^c(\mathbf{q}_N) & \text{if } M_f < 0 \end{cases} \tag{14}$$

where the subscripts O and N refer to the states of the owner and the neighbor cells, respectively. The interface Mach number M_f is computed as:

$$M_f = M_O^+ + M_N^- \tag{15}$$

where:

$$M_k^\pm = \begin{cases} \pm\frac{1}{4}(Ma_k \pm 1)^2 & \text{if } |Ma_k| \leq 1 \\ \frac{1}{2}(Ma_k \pm |Ma_k|) & \text{if } |Ma_k| > 1 \end{cases} \tag{16}$$

with $Ma_k = \frac{\mathbf{U}_k \cdot \mathbf{n}}{a}$, and $k = O/N$. The interface pressure is approximated as:

$$p_f = p_O^+ + p_N^- \tag{17}$$

where $p_k^\pm$ are given by:

$$p_k^\pm = \begin{cases} \frac{1}{4} p_k (Ma_k \pm 1)^2 (2 \mp Ma_k) & \text{if } |Ma_k| \leq 1 \\ \frac{1}{2} p_k \frac{Ma_k \pm |Ma_k|}{Ma_k} & \text{if } |Ma_k| > 1 \end{cases} \tag{18}$$

The interface velocity of the energy source term $([\sigma] \cdot \mathbf{U})_f$ is evaluated as:

$$\mathbf{U}_f = \begin{cases} \mathbf{U}_O & \text{if } M_f \geq 0 \\ \mathbf{U}_N & \text{if } M_f < 0 \end{cases} \tag{19}$$

The spatial reconstruction of the numerical solution that determines the owner and neighbor states is performed using the Van Leer limiter [41], which achieves second order accuracy in space. The time derivative is discretized using the fourth-order Runge–Kutta scheme,

in order to ensure proper temporal accuracy. The Runge–Kutta scheme is constructed by successively applying the Euler method over the four Runge–Kutta steps [15,16,23]:

first step.

$$\mathbf{K}_1 = \mathbf{L}(\overline{\mathbf{q}}^n) \tag{20}$$

$$\overline{\mathbf{q}}^{(1)} = \overline{\mathbf{q}}^n + \frac{\Delta t}{2}\mathbf{K}_1 \tag{21}$$

second step.

$$\mathbf{K}_2 = \mathbf{L}\left(\overline{\mathbf{q}}^{(1)}\right) \tag{22}$$

$$\overline{\mathbf{q}}^{(2)} = \overline{\mathbf{q}}^n + \frac{\Delta t}{2}\mathbf{K}_2 \tag{23}$$

third step.

$$\mathbf{K}_3 = \mathbf{L}\left(\overline{\mathbf{q}}^{(2)}\right) \tag{24}$$

$$\overline{\mathbf{q}}^{(3)} = \overline{\mathbf{q}}^n + \Delta t\mathbf{K}_3 \tag{25}$$

fourth step.

$$\mathbf{K}_4 = \mathbf{L}\left(\overline{\mathbf{q}}^{(3)}\right) \tag{26}$$

$$\overline{\mathbf{q}}^{n+1} = \overline{\mathbf{q}}^n + \Delta t\left(\frac{1}{6}\mathbf{K}_1 + \frac{1}{3}\mathbf{K}_2 + \frac{1}{3}\mathbf{K}_3 + \frac{1}{6}\mathbf{K}_4\right) \tag{27}$$

where $\mathbf{L}(\bullet)$ is the right-hand side of Equation (9).

3. Case Study

The reference experimental injection is presented in [12]. An injector with hole diameter of 0.58 mm, is supplied with hydrogen at nominal pressure of 200 bar, and connected to a low pressure environment, filled with nitrogen (N_2) at 10 bar. A hexahedral-dominant mesh was created using cfMesh, as shown in Figure 1.

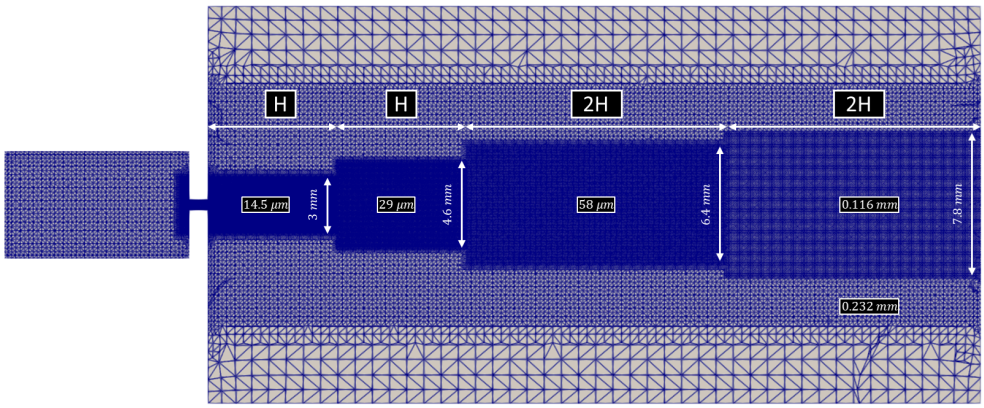


Figure 1. Computational mesh section.

The computational domain consists of a high pressure chamber of radius 6 mm and length 10 mm, and a low pressure environment of radius 10 mm and length of 42 mm. The nozzle is modeled as a cylinder of diameter $d = 0.58$ mm and length $L = 1$ mm. The grid, with a base size of 0.928 mm, is progressively refined toward the nozzle within cylindrical regions. The dimension H is set to $H = 12D$, and the maximum refinement level is 6, resulting in approximately 40 computational cells across the nozzle diameter. This mesh resolution was found to accurately describe the flow field structures, resolving turbulent scales down to approximately the Taylor length scale [15,18]. It is worth noting that the

computational domain extends well beyond the refined region where the flow is accurately resolved. In general, when only a small portion of a larger environment is simulated, appropriate boundary conditions should be imposed. This requires knowledge of the time history of the flow variables at the boundaries, or at least their steady-state values when the transient behavior is not of interest. Since this information is often unavailable, a common practical solution is to place the domain boundaries sufficiently far from the jet to avoid boundary interactions and to prescribe the static pressure of the undisturbed environment, where the fluid remains subsonic. The total number of cells is around 25 millions. Initially, hydrogen occupies the high pressure tank and half of the nozzle at a pressure of 140 bar, corresponding to the effective steady-state injection pressure estimated upstream of the nozzle hole [12]. The rest of the computational domain contains nitrogen at 10 bar. With the employed setup, this numerical model does not simulate the real transient nozzle opening, during which pressure upstream of the nozzle hole and flow rate through it increase progressively. Instead, the model assumes an instant release of a diaphragm separating the high-pressure hydrogen from the low-pressure air, resulting in an instantaneous opening. While this affects the transient phenomena at the start of injection (SOI), there is no influence on the steady-state near-nozzle field under investigation. The initial temperature of both hydrogen and air is equal to 298 K. Total pressure and temperature boundary conditions are prescribed at the inlet of the high pressure chamber, while zero gradient temperature and outlet static pressure are imposed at the low pressure environment boundaries, as the flow is expected to remain subsonic. No slip condition is imposed for velocity at the domain walls. The complete domain boundaries are illustrated in Figure 2, and the corresponding boundary conditions are reported in Table 2.

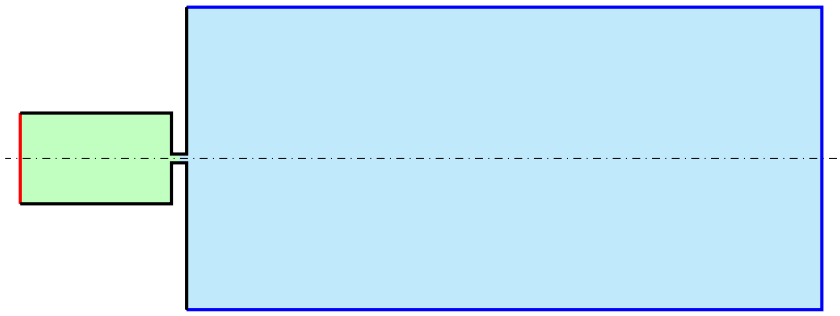


Figure 2. Boundary and initial conditions: inlet (red), outlet (blue) and wall (black). Hydrogen is represented in light green, and nitrogen in cyan.

Table 2. Boundary conditions.

Boundary	Pressure		Temperature		Velocity
	Type	Value	Type	Value	Type
inlet	totalPressure	140 bar	totalTemperature	298 K	zeroGradient
outlet	fixedValue	10 bar	zeroGradient	-	zeroGradient
wall	zeroGradient	-	zeroGradient	-	noSlip

4. Results and Discussion

Two simulations were performed using the KNP scheme available in rhoCentralFoam, enhanced with the Runge–Kutta time integration scheme, and the AUSM scheme, which was newly implemented as described in Section 2. The KNP simulation was considered a reference case, since the same numerical investigation had already been successfully simulated in [15]. The following analysis therefore focuses on the differences between the two solvers in the numerical results, and, more specifically, on the accuracy of the AUSM scheme. Both simulations were performed on two computational nodes, each with 32 cores,

equipped with Intel Xeon 6130 CPUs. The simulation time is approximately 90.5 h for the KNP simulation and 162.9 h for the AUSM one; further improvements of the AUSM scheme implementation in OpenFOAM can reduce the required computational time. Figure 3 shows the temporal evolution of the velocity magnitude obtained using the AUSM scheme, with the steady-state position of the numerical Mach disk indicated by the yellow dotted line (at a distance of 1.347 mm from the nozzle outlet). A spherical shock, known as a bow shock [17], propagates through the quiescent air in Figure 3a, while the hydrogen jet develops more slowly. Figure 3b shows the initial Mach disk, which forms approximately 6 µs after the SOI and moves toward its final position in Figure 3b–f, while its diameter increases. From this point onward, the Mach disk position and structure do not change significantly, while the jet continues to evolve at the tip and in the surrounding flow field, as illustrated in Figure 3g–i. Although this reproduces the reference injection, the experimental transient lasts around 170 µs, which is much slower than in simulations, where the Mach disk reaches its steady position after about 20 µs. This discrepancy, as anticipated in Section 3, was likely caused by the time delay associated with the pressurization of the injector chamber, which was not accounted for in the present simulation. The numerical Schlieren images in Figure 4 are obtained at $t = 25$ µs by computing the magnitude of the density-gradient. Figure 4a shows a magnification of the near-nozzle field of the AUSM simulation result, compared with experimental data here represented as red dots replicating the relevant experimental discontinuities clearly visible in the optical data reported in [12]. The distance of the Mach disk from the nozzle outlet is approximately 1.347 mm for the ASUM simulation, and is very close to the experimental value of 1.345 mm. The AUSM scheme provides a diameter of 0.504 mm, which is a bit larger than the experimental diameter of 0.367 mm. However, AUSM numerical results show satisfactory agreement with experimental data. The Mach disk obtained with the KNP scheme can be observed in Figure 4b, where the KNP (upper half) and the AUSM simulations (lower half) are compared. The position and dimension of the Mach disk in the KNP simulation are 1.347 mm and 0.519 mm, respectively. While both schemes accurately predict the position of the Mach disk, the discrepancies on its diameter appear to be related to an asymmetry in the experimental datum, which is probably caused by reflected pressure waves that are absent in the present simulations, since the shorter simulated transient prevents any wall interaction. Table 3 summarizes the main geometrical features of the numerical and experimental Mach disks.

After reaching choked conditions, the computed mass flow rates are 1.856 g/s and 1.891 g/s for the AUSM and KNP simulations, respectively. A reference value can be obtained from the mass flow rate through an isentropic convergent nozzle at choked conditions [12]:

$$\dot{m} = p^0 C_D A_e \sqrt{\frac{\gamma}{RT^0}} \left(\frac{2}{\gamma + 1} \right)^{\frac{\gamma+1}{2(\gamma-1)}} \tag{28}$$

where p^0 and T^0 are, respectively, the total injection pressure and temperature, A_e is the nozzle exit cross-sectional area, and $C_D = 0.79$ is the discharge coefficient reported in [12]. For $p^0 = 140$ bar and $T^0 = 298$ K, the mass flow rate is equal to 1.805 g/s. In general, Figure 4 highlights the reduced dissipation of the AUSM scheme, which better capture small flow vortices, that tend to be smoothed and dissipated by the KNP scheme. This allows the smaller scales of turbulence to be better resolved—as small vortices are not dissipated—enhancing turbulent mixing. Figure 5 presents the isocontour surfaces of H_2 mass fraction equal to 0.1 at $t = 25$ µs, where the AUSM scheme (green isocontour) predicts a quicker jet penetration and a more intense gas mixing than KNP one (blue isocontour), in the region surrounding the jet. This results in a larger AUSM jet with surface area of 245.176 mm^2 and volume of 40.661 mm^3, compared to 161.473 mm^2 and 40.661 mm^3 for the KNP simulation. The surface-to-volume ratio of the AUSM jet is approximately 52% higher

than that of the KNP jet: the more pronounced wrinkled surface of the jet obtained with the AUSM scheme compared to the KNP one further highlights the reduced numerical diffusion of the former scheme.

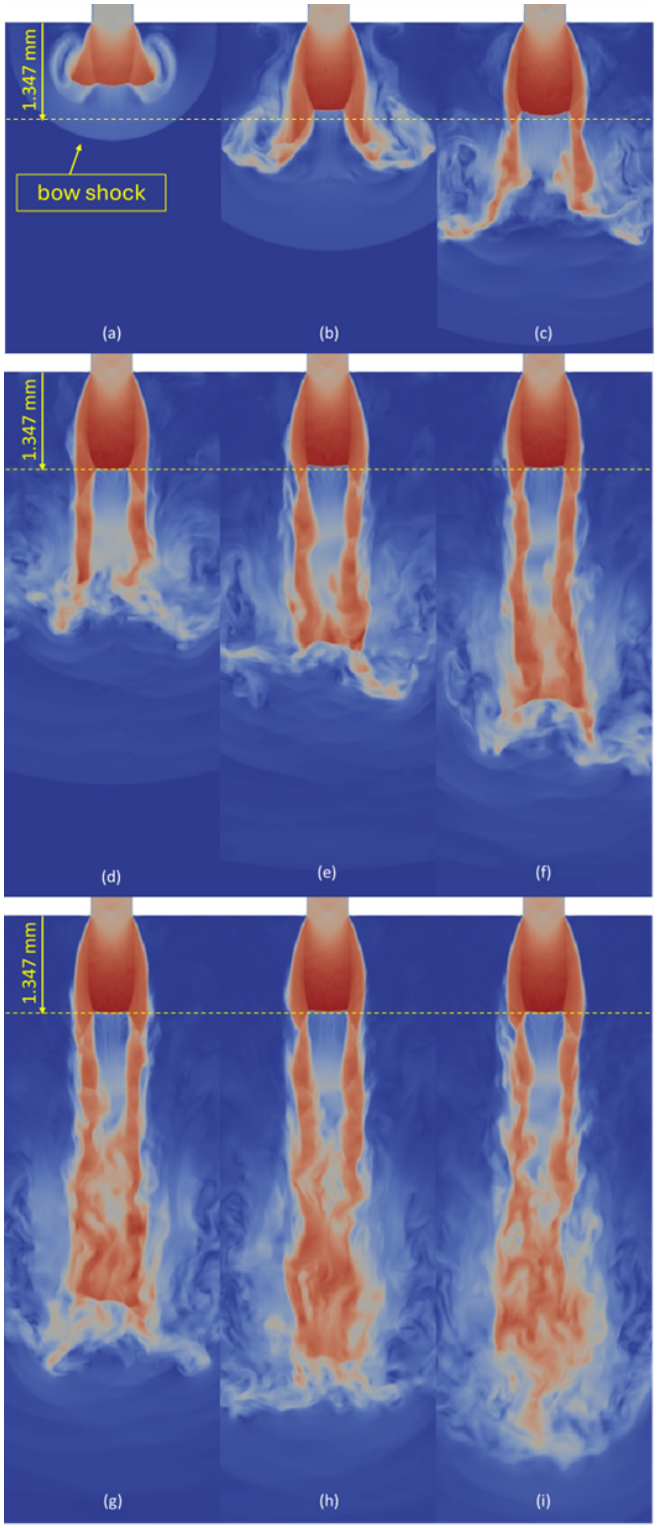
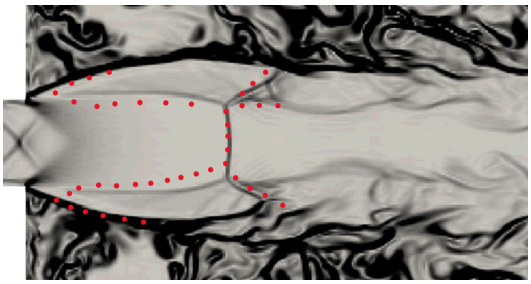
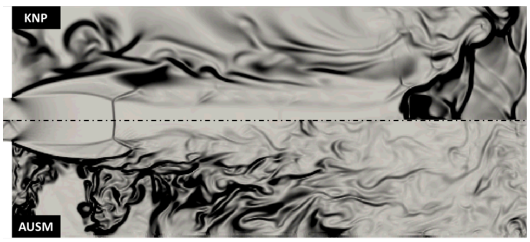


Figure 3. Velocity magnitude time evolution for AUSM simulation: 3 µs (**a**), 6 µs (**b**), 9 µs (**c**), 12 µs (**d**), 15 µs (**e**), 18 µs (**f**), 21 µs (**g**), 23 µs (**h**), and 25 µs (**i**). Red: high velocity, blue: low velocity.



(**a**)



(**b**)

Figure 4. Numerical Schlieren images at 25 µs: (**a**) magnification of the Mach disk for the AUSM simulation (red dots indicate experimental data); (**b**) comparison between KNP (upper half) and AUSM results (lower half).

Table 3. Geometrical features of the Mach disks.

Data	Distance (mm)	Diameter (mm)
Experimental	1.345	0.367
KNP	1.347	0.519
AUSM	1.347	0.504

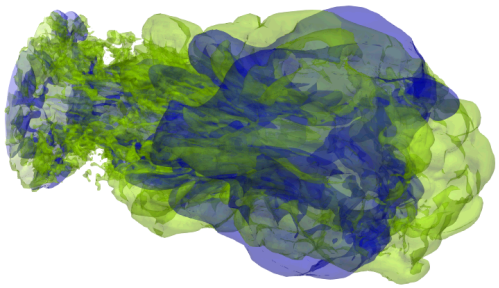


Figure 5. Iso-surfaces of H_2 mass fraction equal to 0.1 at 25 µs: KNP (blue), and AUSM (green).

The analysis of the Scalar Dissipation Rate (SDR) confirms the higher mixing activity involving the AUSM simulation. The SDR of a scalar c is defined as [42,43]:

$$\chi = 2\mathcal{D}_c \|\nabla c\|^2 \tag{29}$$

where $\mathcal{D}_c$ is the mixture fraction diffusivity. Figure 6 shows the $log_{10}(\chi/\chi_{ref})$ of the H_2 mass fraction, where $\chi_{ref} = 2\mathcal{D}_{ref}\left(\frac{c_{max}}{D}\right)^2$, with $c_{max} = 1$ and $\mathcal{D}_{ref}$ is the reference diffusivity of the far field [43]. The SDR field is quite uniform in the KNP simulation, with a well-defined surface that delimits the hydrogen jet from the surrounding nitrogen. The low SDR values do not indicate that mixing has already occurred, but rather that the mixing process is just starting. In contrast, this surface is wider and more corrugated in the AUSM simulation, indicating that mixing involves a larger amount of air. The high SDR values, comparable to those observed in the KNP simulation, suggest that the mixing process is still ongoing.

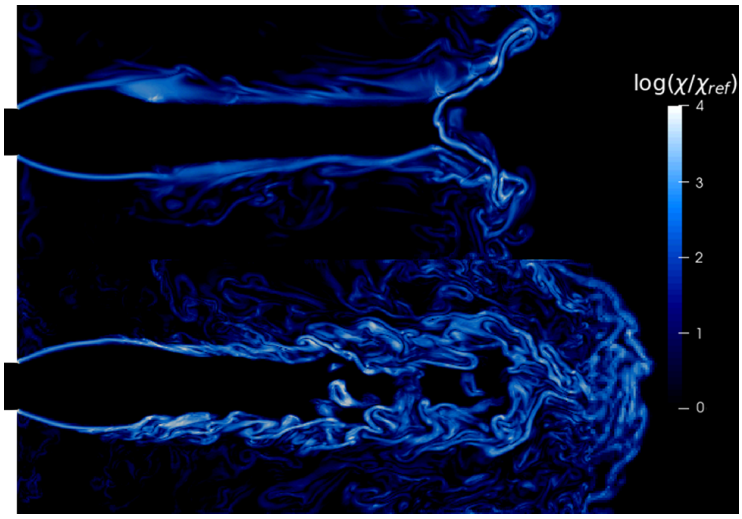
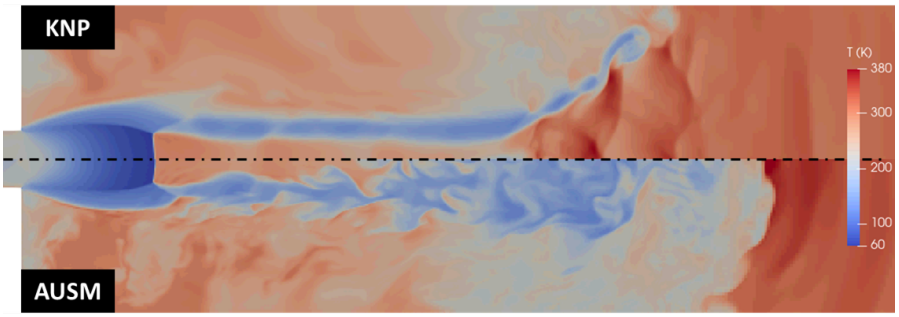
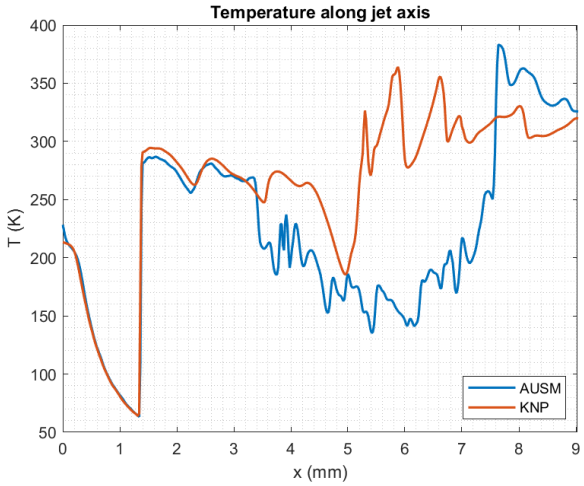


Figure 6. SDR of H_2 mass fraction at 25 µs: KNP scheme (**top**), and AUSM scheme (**bottom**).

These results demonstrate the superior accuracy of the AUSM scheme for multi-component supersonic flows, outperforming the KNP scheme and providing a more detailed representation of the flow field. Despite its higher computational cost, the AUSM scheme offers a favorable trade-off between accuracy, applicability to real-gas models, and computational efficiency, making it a suitable density-based solver for the OpenFOAM library [29,31,32]. Figure 7 compares the temperature fields computed with the AUSM scheme (upper half) and the KNP scheme (lower half), while the temperature along the jet axis of the two simulations is shown in Figure 7b. Hydrogen undergoes an intense expansion at the nozzle exit, leading to the formation of a low-temperature region, where the hydrogen temperature drops to approximately 60 K. The minimum temperature is similar for both models, while more pronounced differences are observed at the nozzle outlet and downstream of the Mach disk. The former are attributed to oscillations inside the nozzle, where shocks originate at the nozzle's sharp edges and subsequently reflect further along the walls; the latter result from a different mixing between the hot N_2 and the cold H_2. The use of a real gas model could improve accuracy, as the ideal gas model is not suitable for describing gases at such low temperatures, particularly hydrogen, which has a negative Joule–Thomson coefficient [17]. On the other hand, the present authors note that the JANAF polynomials are not valid for calculating specific heat under these conditions, as the gas temperature is well below the lower JANAF temperature limit, which typically corresponds to ambient temperature. Therefore, an appropriate specific heat model should be established, regardless of the gas model used. Nevertheless, the ideal gas model and the constant specific heat assumption still provide an accurate description of the Mach disk structure. The Mach number is presented in Figure 8a, where both the KNP (upper half) and the AUSM scheme (lower half) provide a Mach number around 1.4 at the nozzle outlet. According to [44], a supersonic flow in a convergent duct can be attributed to the formation of a boundary layer inside the channel. Figure 8b shows the magnification of the Mach field inside the nozzle. In both simulations, a thin boundary layer detaches from the nozzle wall as a result of the abrupt variation in nozzle cross-section. The boundary layer reduces the effective cross-sectional area of the nozzle, forming a convergent-divergent geometry that accelerates the flow to supersonic velocities. The boundary layer is slightly thicker in the KNP simulation.

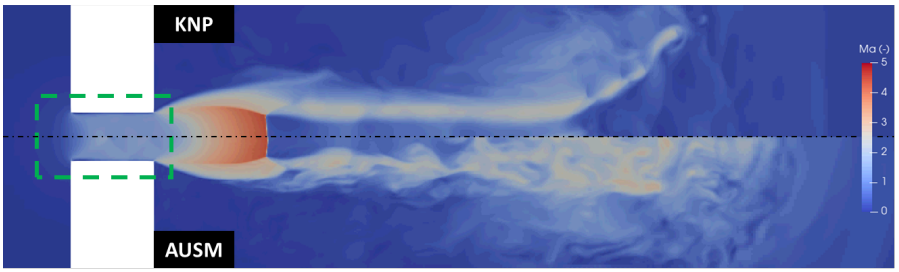


(**a**)

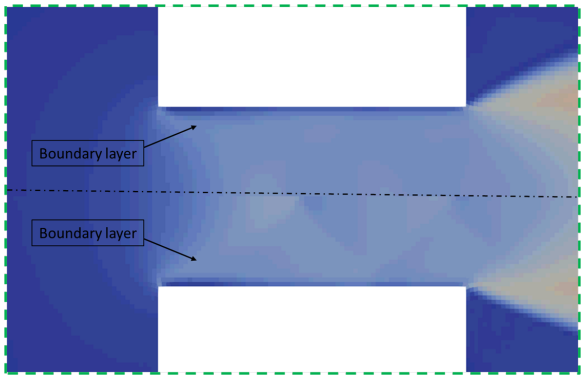


(**b**)

Figure 7. (**a**) Temperature fields at 25 µs of KNP (upper half) and AUSM (lower half); (**b**) temperature along jet axis of KNP (red) and AUSM (blue).



(**a**)



(**b**)

Figure 8. (**a**) Mach field at 25 µs, and (**b**) zoom of the Mach field inside the nozzle of KNP (upper half) and AUSM (lower half).

5. Conclusions

The AUSM scheme was implemented in an OpenFOAM library. The solver was successfully validated against an experimental under-expanded H_2 injection from the literature. The numerical model accurately captured the near-nozzle field and the results were in satisfactory agreement with other CFD investigations in the literature. The numerical results were compared with those computed with the KNP scheme, which is commonly used for simulating under-expanded jets in OpenFOAM. The Mach disk structure was well reproduced by both schemes, whereas more pronounced differences were observed in the flow field downstream of and surrounding the disk. The lower dissipation of the AUSM scheme resulted in a significantly higher turbulence intensity, which increased the jet penetration and enhanced the gas mixing. Specifically, the isocontour surfaces of the hydrogen mass fraction revealed a larger jet volume and surface, as well as a higher surface to volume ratio, while the SDR confirmed the higher mixing activity. In conclusion, the present work demonstrated the superior performance of the AUSM scheme and proposed it as an alternative numerical method for the simulation of multi-component supersonic flows within the OpenFOAM environment.

Author Contributions: Conceptualization, O.V.; methodology, A.F., O.V. and C.B.; software, C.B.; validation, C.B.; formal analysis, O.V. and C.B.; investigation, O.V. and C.B.; resources, A.F.; data curation, C.B.; writing—original draft preparation, C.B.; writing—review and editing, A.F. and O.V.; visualization, C.B.; supervision, A.F. and O.V.; project administration, A.F.; funding acquisition, A.F. All authors have read and agreed to the published version of the manuscript.

Funding: This publication is part of the project PNRR-NGEU which has received funding from the MUR—DM 118/2023.

Data Availability Statement: The original contributions presented in this study are included in the article. Further inquiries can be directed to the corresponding author.

Acknowledgments: Computational resources provided by HPC@PoliTO, www.hpc.polito.it (accessed on 4 February 2026).

Conflicts of Interest: Authors have no known competing financial interests or personal relationship that could have appeared to influence the work reported in this paper.

Abbreviations

The following abbreviations are used in this manuscript:

AUSM	Advection Upwind Splitting Method
AMR	Adaptative Mesh Refinement
CFD	Computational Fluid Dynamics
DI	Direct Injection
HPDI	High Pressure Direct Injection
H2ICEs	H_2 Internal Combustion Engines
IVC	Intake Valve Closure
KNP	Kurganov–Noelle–Petrova
LES	Large Eddy Simulation
LPDI	Low Pressure Direct Injection
PFI	Port Fuel Injection
SDR	Scalar Dissipation Rate
SOI	Start Of Injection
WALE	Wall Adaptative Large Eddy
WENO	Weighted Essentially Non Oscillatory

References

1. Stępień, Z. A comprehensive overview of hydrogen-fueled internal combustion engines: Achievements and future challenges. *Energies* **2021**, *14*, 6504. [CrossRef]
2. Hu, Z.; Yuan, S.; Wei, H.; Huang, Z.; Wei, H.; Chan, S.H.; Zhou, L. High-pressure injection or low-pressure injection for a direct injection hydrogen engine? *Int. J. Hydrogen Energy* **2024**, *59*, 383–389. [CrossRef]
3. Pavan, N.; Cicalese, G.; Gestri, L.; Fontanesi, S.; Breda, S.; Mechi, M.; Vongher, S.; Postrioti, L.; Buitoni, G.; Martino, M. Effects of Jet Caps on Hydrogen Piezoelectric Injectors for DI Applications: Experiments and 3D-CFD Simulations. In *Proceedings of the WCX SAE World Congress Experience*; SAE Technical Paper; SAE International: Warrendale, PA, USA, 2025.
4. Onorati, A.; Payri, R.; Vaglieco, B.M.; Agarwal, A.K.; Bae, C.; Bruneaux, G.; Canakci, M.; Gavaises, M.; Günthner, M.; Hasse, C.; et al. The role of hydrogen for future internal combustion engines. *Int. J. Engine Res.* **2022**, 23, *529–540. [CrossRef]*
5. Merotto, L.; Balmelli, M.; Soltic, P. Hydrogen direct injection: Optical investigation of premixed and jet-guided combustion modes. *Int. J. Hydrogen Energy* **2024**, *61*, 284–295. [CrossRef]
6. Liu, X.; Srna, A.; Yip, H.L.; Kook, S.; Chan, Q.N.; Hawkes, E.R. Performance and emissions of hydrogen-diesel dual direct injection (H2DDI) in a single-cylinder compression-ignition engine. *Int. J. Hydrogen Energy* **2021**, *46*, 1302–1314. [CrossRef]
7. Liu, X.; Yang, L.; Chan, Q.N.; Kook, S. Split injection strategies for a high-pressure hydrogen direct injection in a small-bore dual-fuel diesel engine. *Int. J. Hydrogen Energy* **2024**, *57*, 904–917. [CrossRef]
8. Kim, S.; Lee, J.; Lee, S.; Lee, S.; Kim, K.; Min, K. Effects of various compression ratios on a direct injection spark ignition hydrogen-fueled engine in a single-cylinder engine. *Int. J. Automot. Technol.* **2024**, *25*, 1159–1172. [CrossRef]
9. Park, C.; Kim, Y.; Oh, S.; Oh, J.; Choi, Y.; Baek, H.; Lee, S.W.; Lee, K. Effect of fuel injection timing and injection pressure on performance in a hydrogen direct injection engine. *Int. J. Hydrogen Energy* **2022**, *47*, 21552–21564. [CrossRef]
10. Ferrari, A.; Pizzo, P. *Injection Technologies and Mixture Formation Strategies for Spark Ignition and Dual-Fuel Engines*; SAE International: Warrendale, PA, USA, 2022.
11. Ferrari, A. *Fondamenti di Termofluidodinamica per le Macchine*; CittàStudiEdizioni: Novara, Italy, 2020.
12. Yip, H.L.; Srna, A.; Liu, X.; Kook, S.; Hawkes, E.R.; Chan, Q.N. Visualization of hydrogen jet evolution and combustion under simulated direct-injection compression-ignition engine conditions. *Int. J. Hydrogen Energy* **2020**, *45*, 32562–32578. [CrossRef]
13. Falfari, S.; Cazzoli, G.; Mariani, V.; Bianchi, G.M. Hydrogen application as a fuel in internal combustion engines. *Energies* **2023**, *16*, 2545. [CrossRef]
14. Gurri, S.; Vento, O.; Marello, O.; Finesso, R.; Gallo, A.; Vargiu, L.; Ferrari, A. A methodology for boundary condition optimization in 3D-CFD of internal combustion engines. *Appl. Therm. Eng.* **2026**, *292*, 130270. [CrossRef]
15. Duronio, F.; De Vita, A. CFD analysis of hydrogen and methane turbulent transitional under-expanded jets. *Int. J. Heat Fluid Flow* **2024**, *107*, 109381. [CrossRef]
16. Duronio, F.; Ranieri, S.; Mascio, A.D.; Vita, A.D. Simulation of high pressure, direct injection processes of gaseous fuels by a density-based OpenFOAM solver. *Phys. Fluids* **2021**, *33*, 066104. [CrossRef]
17. Hamzehloo, A.; Aleiferis, P. Large eddy simulation of near-nozzle shock structure and mixing characteristics of hydrogen jets for direct-injection spark-ignition engines. In Proceedings of the International Conference on Heat Transfer, Fluid Mechanics and Thermodynamics, Orlando, FL, USA, 14–16 July 2014.
18. Hamzehloo, A.; Aleiferis, P. Gas dynamics and flow characteristics of highly turbulent under-expanded hydrogen and methane jets under various nozzle pressure ratios and ambient pressures. *Int. J. Hydrogen Energy* **2016**, *41*, 6544–6566. [CrossRef]
19. Hamzehloo, A.; Aleiferis, P. Numerical modelling of transient under-expanded jets under different ambient thermodynamic conditions with adaptive mesh refinement. *Int. J. Heat Fluid Flow* **2016**, *61*, 711–729. [CrossRef]
20. Franquet, E.; Perrier, V.; Gibout, S.; Bruel, P. Free underexpanded jets in a quiescent medium: A review. *Prog. Aerosp. Sci.* **2015**, *77*, 25–53. [CrossRef]
21. Allocca, L.; Montanaro, A.; Meccariello, G.; Duronio, F.; Ranieri, S.; De Vita, A. *Under-eXpanded Gaseous Jets Characterization for Application in Direct Injection Engines: Experimental and Numerical Approach*; Technical Report, SAE Technical Paper; SAE International: Warrendale, PA, USA, 2020.
22. Zaghi, S.; Di Mascio, A.; Favini, B. Application of WENO-positivity-preserving schemes to highly under-expanded jets. *J. Sci. Comput.* **2016**, *69*, 1033–1057. [CrossRef]
23. Vuorinen, V.; Keskinen, J.P.; Duwig, C.; Boersma, B.J. On the implementation of low-dissipative Runge–Kutta projection methods for time dependent flows using OpenFOAM®. *Comput. Fluids* **2014**, *93*, 153–163. [CrossRef]
24. Liou, M.S.; Steffen, C.J., Jr. A new flux splitting scheme. *J. Comput. Phys.* **1993**, *107*, 23–39. [CrossRef]
25. Liou, M.S. A sequel to ausm: Ausm+. *J. Comput. Phys.* **1996**, *129*, 364–382. [CrossRef]
26. Liou, M.S. A sequel to AUSM, Part II: AUSM+-up for all speeds. *J. Comput. Phys.* **2006**, *214*, 137–170. [CrossRef]
27. Kitamura, K.; Liou, M.S.; Chang, C.H. Extension and comparative study of AUSM-family schemes for compressible multiphase flow simulations. *Commun. Comput. Phys.* **2014**, *16*, 632–674. [CrossRef]

28. Zang, B.; US, V.; New, T.H.D. OpenFOAM based numerical simulation study of an underexpanded supersonic jet. In Proceedings of the 55th AIAA Aerospace Sciences Meeting, Grapevine, TX, USA, 9–13 January 2017; p. 0747.
29. Arya, N.; Bhaduri, S.; De, A. Acoustic characteristics of supersonic planar impinging jets. *Eur. J. -Mech.-B/Fluids* **2023**, *102*, 56–79. [CrossRef]
30. Modesti, D.; Pirozzoli, S. A low-dissipative solver for turbulent compressible flows on unstructured meshes, with OpenFOAM implementation. *Comput. Fluids* **2017**, *152*, 14–23. [CrossRef]
31. Duronio, F.; Di Mascio, A. Implementation and assessment of a low-dissipative OpenFOAM solver for compressible multi-species flows. *Comput. Fluids* **2024**, *274*, 106240. [CrossRef]
32. Jiang, C.; Pan, J.; Zhu, Y.; Li, J.; Quaye, E.K. Development and verification of a high-speed compressible reactive flow solver in OpenFOAM. *J. Comput. Sci.* **2022**, *63*, 101780. [CrossRef]
33. Greenshields, C.J.; Weller, H.G.; Gasparini, L.; Reese, J.M. Implementation of semi-discrete, non-staggered central schemes in a colocated, polyhedral, finite volume framework, for high-speed viscous flows. *Int. J. Numer. Methods Fluids* **2010**, *63*, 1–21. [CrossRef]
34. Kurganov, A.; Noelle, S.; Petrova, G. Semidiscrete central-upwind schemes for hyperbolic conservation laws and Hamilton–Jacobi equations. *SIAM J. Sci. Comput.* **2001**, *23*, 707–740. [CrossRef]
35. Marcantoni, L.G.; Elaskar, S.; Tamagno, J.; Saldía, J.; Krause, G. An assessment of the OpenFOAM implementation of the KNP scheme to simulate strong explosions. *Shock Waves* **2021**, *31*, 193–202. [CrossRef]
36. Chase, M.W. NIST-JANAF thermochemical tables. *J. Phys. Chem. Ref. Data* **1998**, *28*, 1951.
37. Vuorinen, V.; Yu, J.; Tirunagari, S.; Kaario, O.; Larmi, M.; Duwig, C.; Boersma, B. Large-eddy simulation of highly underexpanded transient gas jets. *Phys. Fluids* **2013**, *25*, 016101. [CrossRef]
38. Sutherland, W. LII. The viscosity of gases and molecular force. *Lond. Edinb. Dublin Philos. Mag. J. Sci.* **1893**, *36*, 507–531. [CrossRef]
39. Nicoud, F.; Ducros, F. Subgrid-scale stress modelling based on the square of the velocity gradient tensor. *Flow Turbul. Combust.* **1999**, *62*, 183–200. [CrossRef]
40. Toro, E.F. *Riemann Solvers and Numerical Methods for Fluid Dynamics: A Practical Introduction*; Springer Science & Business Media: Berlin/Heidelberg, Germany, 2013.
41. Van Leer, B. Towards the ultimate conservative difference scheme. II. Monotonicity and conservation combined in a second-order scheme. *J. Comput. Phys.* **1974**, *14*, 361–370. [CrossRef]
42. Duronio, F.; Montanaro, A.; Ranieri, S.; Allocca, L.; De Vita, A. Under-expanded jets characterization by means of cfd numerical simulation using an open foam density-based solver. In *Proceedings of the 15th International Conference on Engines & Vehicles*; SAE Technical Paper; SAE International: Warrendale, PA, USA, 2021.
43. Yu, J.; Vuorinen, V.; Kaario, O.; Sarjovaara, T.; Larmi, M. Visualization and analysis of the characteristics of transitional underexpanded jets. *Int. J. Heat Fluid Flow* **2013**, *44*, 140–154. [CrossRef]
44. Afroosheh, M.; Vakilimoghaddam, F.; Paraschivoiu, M. Boundary layer effects on the critical nozzle of hydrogen sonic jet. *Int. J. Hydrogen Energy* **2017**, *42*, 7440–7446. [CrossRef]

Disclaimer/Publisher's Note: The statements, opinions and data contained in all publications are solely those of the individual author(s) and contributor(s) and not of MDPI and/or the editor(s). MDPI and/or the editor(s) disclaim responsibility for any injury to people or property resulting from any ideas, methods, instructions or products referred to in the content.